FULL PAPER

Lithium Ion Batteries

ADVANCED
ENERGY
MATERIALS

www.advenergymat.de

Low-Temperature Reduction Strategy Synthesized Si/Ti$_3$C$_2$ MXene Composite Anodes for High-Performance Li-Ion Batteries

Xiaobin Hui, Ruizheng Zhao, Peng Zhang, Caixia Li, Chengxiang Wang,* and Longwei Yin*

Silicon is attracting enormous attention due to its theoretical capacity of 4200 mAh g^{-1} as an anode for Li-ion batteries (LIBs). It is of fundamental importance and challenge to develop low-temperature reaction route to controllably synthesize Si/Ti$_3$C$_2$ MXene LIBs anodes. Herein, a novel and efficient strategy integrating in situ orthosilicate hydrolysis and a low-temperature reduction process to synthesize Si/Ti$_3$C$_2$ MXene composites is reported. The hydrolysis of tetraethyl orthosilicate leads to homogenous nucleation and growth of SiO$_2$ nanoparticles on the surface of Ti$_3$C$_2$ MXene. Subsequently, SiO$_2$ nanoparticles are reduced to Si via a low-temperature (200 °C) reduction route. Importantly, Ti$_3$C$_2$ MXene not only provides fast transfer channels for Li$^+$ and electrons, but also relieves volume expansion of Si during cycling. Moreover, the characteristics of excellent pseudocapacitive performance and high conductivity of Ti$_3$C$_2$ MXene can synergistically contribute to the enhancement of energy storage performance. As expected, Ti$_3$C$_2$/Si anode exhibits an outstanding specific capacity of 1849 mAh g^{-1} at 100 mA g^{-1}, even retaining 956 mAh g^{-1} at 1 A g^{-1}. The low-temperature synthetic route to Si/Ti$_3$C$_2$ MXene electrodes and involved battery-capacitive dual-model energy storage mechanism has potential in the design of novel high-performance electrodes for energy storage devices.

1. Introduction

Silicon (Si) is one of the most promising anode materials for next-generation lithium-ion batteries (LIBs), due to its high theoretical capacity (4200 mAh g^{-1}), relatively low discharge potential (<0.5 V vs Li/Li$^+$), and abundant earth reserves.[1–3] However, the commercialization of Si anodes for LIBs has always been stuck by rapid capacity fading resulted from the unavoidable large volume expansion and the intrinsically poor electrical conductivity of Si.[4–9] Tremendous efforts have been made to improve the performance of Si-based LIBs, such as fabricating Si particles with nanoscale size,[10] constructing a variety of nanostructures.[11–14] According to the diffusion equation, $\tau = l^2/D$ (where D is the diffusion coefficient, τ is the diffusion time, l is the diffusion length), the nanoscale size can be useful to effectively shorten lithium ion (Li$^+$) diffusion path.[15,16] Besides, nanoscale sized materials have been demonstrated to minimize the mechanical reaction strains caused by the volume expansion during the electrochemical cycles, leading to a significantly enhanced cycling stability.[16,17] However, as for pure Si anodes, Si nanoparticles tend to aggregate to form particle clusters in charge/discharge process, which would lose the advantage of nanostructure with high surface-area-to-volume ratio.[18] Therefore, carbon nanomaterials are usually utilized to support Si particles to solve this nodus, which can not only prevent the aggregation and pulverization of Si nanoparticles, but also enhance the electrical conductivity of the electrode remarkably.[19–24] Among carbon materials, graphene is favorable owing to its two dimensional (2D) merits such as excellent electrical conductivity, large specific surface area, and optimizable interface contact.[25,26] For instance, Xu et al.[27] reported SiO$_x$@graphene composites by encapsulating SiO$_x$ nanoparticles into a self-assembled graphene bubble films, showing excellent Li$^+$ storage performance with a high reversible capacity of 1275 mAh g^{-1} at the current density of 0.1 A g^{-1}.

Nevertheless, the slow Li$^+$ transport rate and poor redox reaction dynamics result in a low capacity contribution of graphene. In this regard, 2D Ti$_3$C$_2$ MXene is an ideal alternative due to its high diffusion mobility of Li$^+$ ions ($\approx$10^{-10}–10^{-9} cm^2 s^{-1})[28] with lower Li$^+$ diffusion barrier (0.07 eV) than that of graphene (0.3 eV).[29,30] Ti$_3$C$_2$ MXene also has been an attractive candidate for electrode materials of supercapacitors[31,32] and anodes of LIBs[33–36] due to the abundant surface redox reaction, which enables Ti$_3$C$_2$ display significant contribution to the capacity rather than only work as conductive matrix. For instance, black phosphorus quantum dot (BPQD)/Ti$_3$C$_2$ MXene nanosheet composites synthesized by an interfacial assembly strategy present a high reversible capacity of 1124 mAh g^{-1} at 50 mA g^{-1}

Dr. X. Hui, Dr. R. Zhao, Dr. P. Zhang, Dr. C. Li, Dr. C. Wang, Prof. L. Yin
Key Laboratory for Liquid-Solid Structural Evolution
and Processing of Materials
Ministry of Education
School of Materials Science and Engineering
Shandong University
Jinan 250061, P. R. China
E-mail: wcxmat@sdu.edu.cn; yinlw@sdu.edu.cn

The ORCID identification number(s) for the author(s) of this article can be found under https://doi.org/10.1002/aenm.201901065.

when used as anodes of LIBs, which is attributed to the excellent conductivity of Ti_3C_2 MXene and indispensable synergies of BPQD and Ti_3C_2 MXene in capacity contribution.[37] Therefore, Ti_3C_2 MXene is expected to replace graphene to combine with Si as LIBs anodes with more excellent electrochemical performance.

Kong et al.[38] first reported $Si@Ti_3C_2$ nanocomposites anodes prepared via ultrasonic mixing of Si powder and Ti_3C_2, only showing a capacity of 188 mAh g^{-1} and poor cycling stability. The main possible problem is that this deposition process of Si is less controllable, and it is hard to form a solid contact between Si nanoparticles and Ti_3C_2 MXene. Zhang et al.[39] prepared Si/MXene composites by mechanically mixing Si particles with MXene ink to achieve high Si loading content, but the aggregation of Si particles may exert a negative effect in enhancing electrochemical performance. $MXene/Si@SiO_x@C$ composite is reported by Guo et al. as electrode for LIBs,[40] exhibiting high electrochemical performance. However, the energy storage mechanism of the $MXene/Si@SiO_x@C$ composite is not discussed and not well understood.

To make full of advantages of MXene and Si, several critical points should be paid attention. First, Si or its precursor (e.g., SiO_2) should be prepared in a controllable way to obtain a monodispersed state. Second, the two building blocks should form a chemical bonding, such as covalent bond to enhance the interfacial charge transfer kinetics. Finally, a mild synthetic

condition is necessary to prevent the damage for the 2D ultrathin layered structure of Ti_3C_2 MXene. It is of great challenge and fundamental importance to develop an efficient low-temperature strategy to homogeneously couple Si with MXene for high-performance anodes for LIBs.

Herein, we synthesized a novel hierarchical porous MXene Ti_3C_2/Si nanocomposite as the anode of LIBs via a controllable hydrolysis of tetraethyl orthosilicate (TEOS) and a low temperature magnesiothermic reduction reaction (LTMRR) at relatively mild reaction conditions (≈200 °C). Monodispersed Si nanoparticles are prepared with uniform diameter around 40 nm, and anchored on Ti_3C_2 nanosheets through Si−O−Ti bonds. The rationally designed structure presents outstanding electrochemical performance with high specific capacity of 1475 mAh g^{-1} at 100 mA g^{-1} after 200 cycles, excellent rate performance of 467 mAh g^{-1} even at 2 A g^{-1}, and superior long cycle life (973 mAh g^{-1} at 1 A g^{-1} after 800 cycles). In addition, the pseudocapacitive behavior of Ti_3C_2 MXene plays an important role in capacity contribution.

2. Results and Discussion

The preparation process of 2D Ti_3C_2/Si nanocomposites is schematically presented in **Figure 1**. Initially, the negatively charged Ti_3C_2 MXene nanosheets are prepared via a HF etching
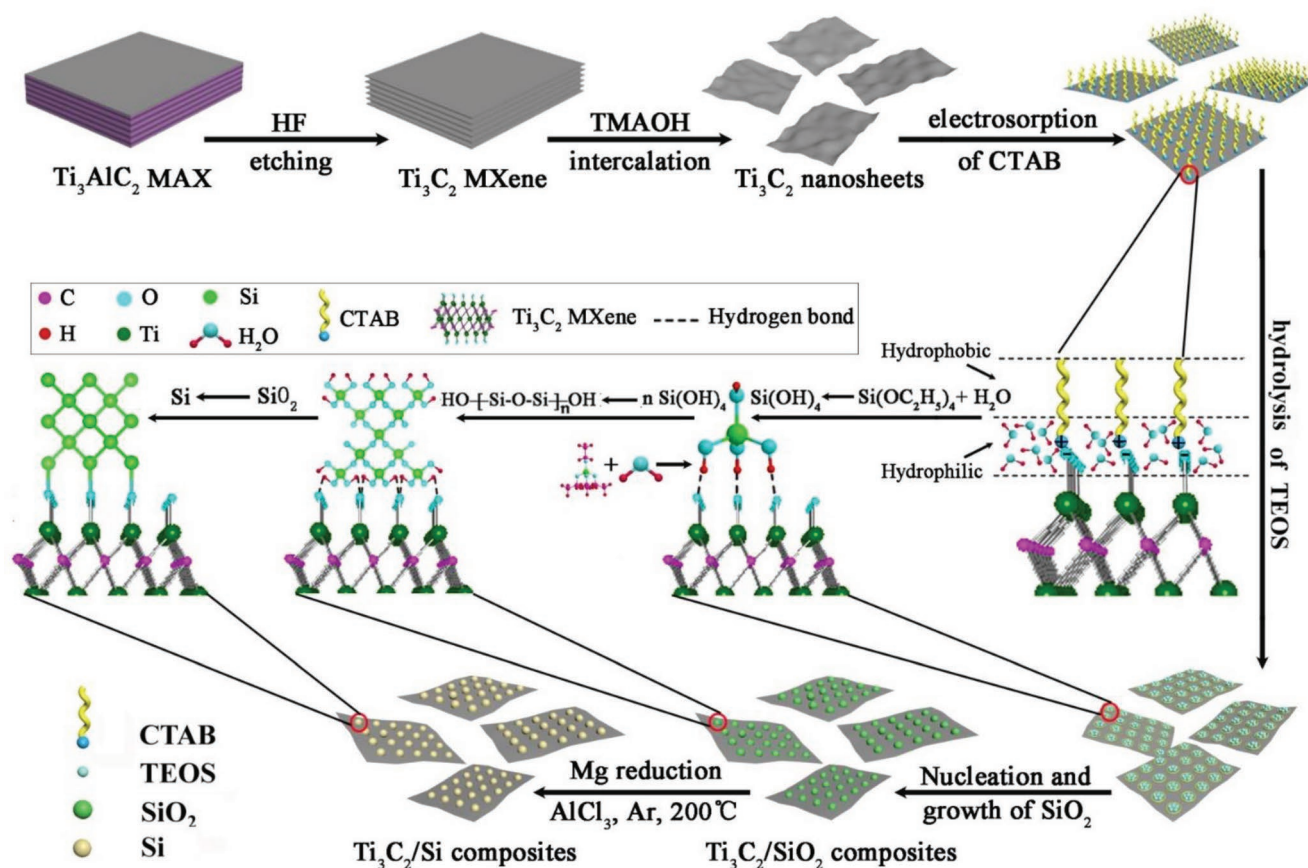

**Figure 1.** The schematic illustration for the synthetic procedure of the Ti_3C_2/Si composite.

(et-Ti$_3$C$_2$) and tetramethyl-ammonium (TMAOH) intercalation (in-Ti$_3$C$_2$) process.[41] Then, cetyltrimethyl lammonium bromide (CTAB), a frequently used structure directing agent,[42] is introduced through the electrostatic interaction between the positively charged amino-group of CTAB and the negatively charged MXene, providing the reaction sites for the hydrolysis of TEOS.[43] According to the water angle test (Figure S1, Supporting Information), the increase of contact angle suggests the formation of hydrophobic region on the surface of treated Ti$_3$C$_2$ MXene nanosheets, while the hydrophobic groups of CTAB stretch upward. Afterward, added TEOS are converted into HO—[—Si—O—Si—]$_n$—OH by hydrolysis and polymerization reaction, inducing the heterogeneous nucleation and growth of SiO$_2$ on the surface of Ti$_3$C$_2$ MXene.[43] The surface of the formed SiO$_2$ particles is covered by hydroxyl groups, which can form hydrogen bond with oxygenic functional groups of Ti$_3$C$_2$ MXene. Subsequently, Ti$_3$C$_2$/Si composites are formed via an LTMRR route using Mg as a reducing agent and AlCl$_3$ as a heat scavenger at a temperature of 200 °C under argon atmosphere (2Mg + SiO$_2$ + 6AlCl$_3$ → 2MgAl$_2$Cl$_8$ + 2AlOCl + Si).[44] The relatively mild condition of LTMRR is beneficial for the maintenance of the lamellar structure of MXene. The two building blocks in the composite are combined by Si—O—Ti, which is confirmed by Fourier transform infrared (FTIR) (Figure 3b) in the later characterization.

The morphology and microstructure of the synthesized Ti$_3$C$_2$/Si nanocomposites are characterized via field emission scanning electron microscopy (FE-SEM) and transmission electron microscopy (TEM). **Figure 2**a reveals an accordion-like multilayer nanostructure, indicating the successful etching of densely packed Ti$_3$AlC$_2$. After TMAOH intercalation and ultrasonic processing, few-layered Ti$_3$C$_2$ nanosheets are obtained (Figure 2b; Figure S2, Supporting Information), which bear a negatively charged state. The atomic force microscope results (Figure S3, Supporting Information) indicate that the thickness of each Ti$_3$C$_2$ nanosheet is around 4.0 nm, corresponding to bilayer.[45] Therefore, cationic surfactant CTAB can be adsorbed on MXene and works as the molecular template for subsequent controllable nucleation and growth of monodispersed SiO$_2$ nanoparticles on the surface of Ti$_3$C$_2$ MXene[43] (Figure 2c). And then SiO$_2$ nanoparticles are reduced to Si (**Figure 3**a) in the LTMRR process, two important features should be pointed out: (1) the formed Si nanoparticles keep a homogenous dispersion; (2) Ti$_3$C$_2$ MXene keeps well lamellar structure (Figure 2d). Both of them are necessary to take advantage of both components. The microstructures of Ti$_3$C$_2$/Si composite are further revealed by low- and high-magnification TEM images (Figure 2e,f), displaying a uniform distribution of Si nanoparticles with an average diameter of 30–40 nm on the surface of MXene nanosheets. An HRTEM
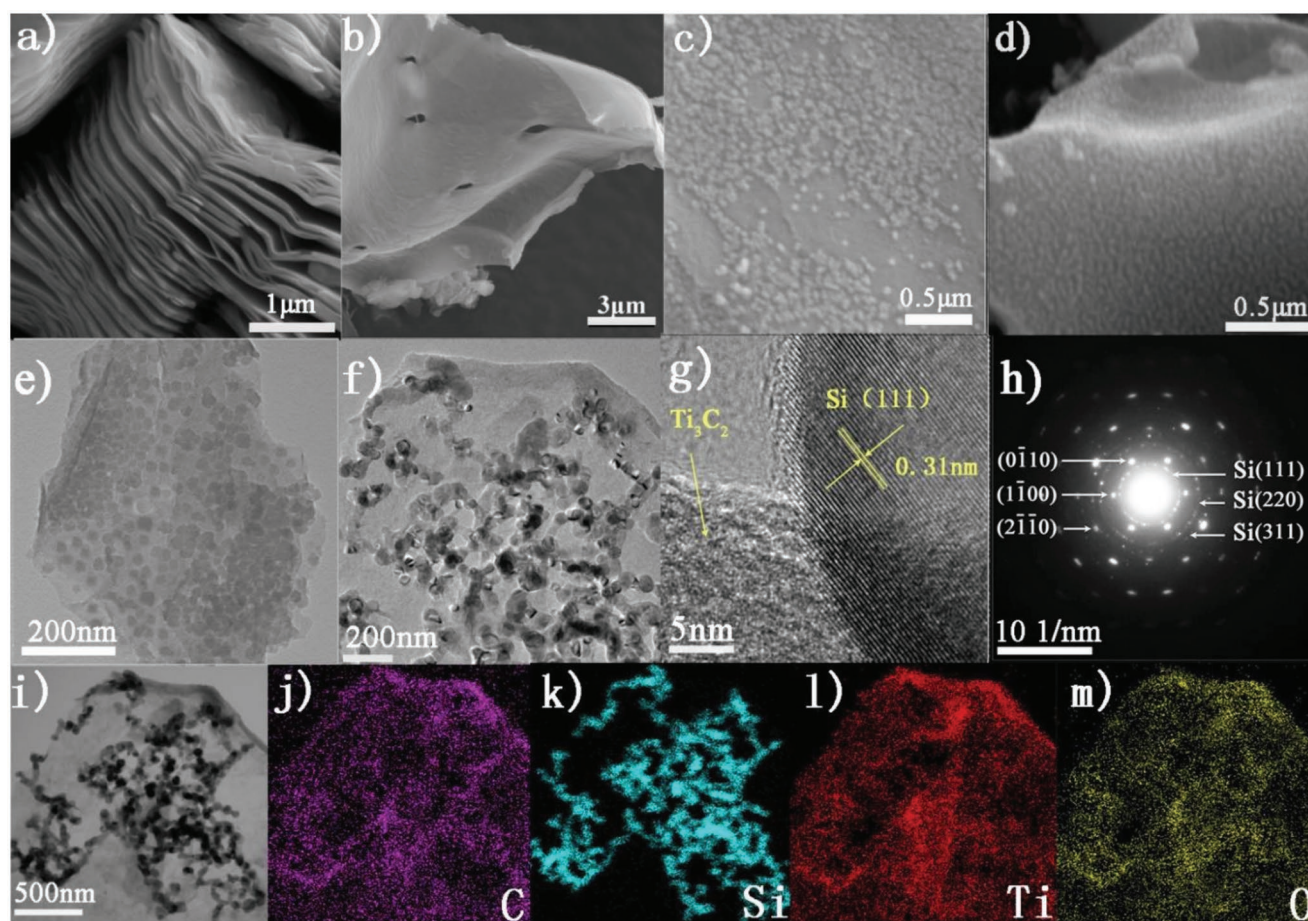
Figure 2. Morphological characterization of Ti$_3$C$_2$/Si nanosheets. Typical SEM image of a) et-Ti$_3$C$_2$, b) in-Ti$_3$C$_2$, c) Ti$_3$C$_2$/SiO$_2$, and d) Ti$_3$C$_2$/Si. e,f) TEM images of Ti$_3$C$_2$/Si. g) HRTEM image of Ti$_3$C$_2$/Si. h) SAED pattern of Ti$_3$C$_2$/Si. i–m) TEM image and elements mappings.
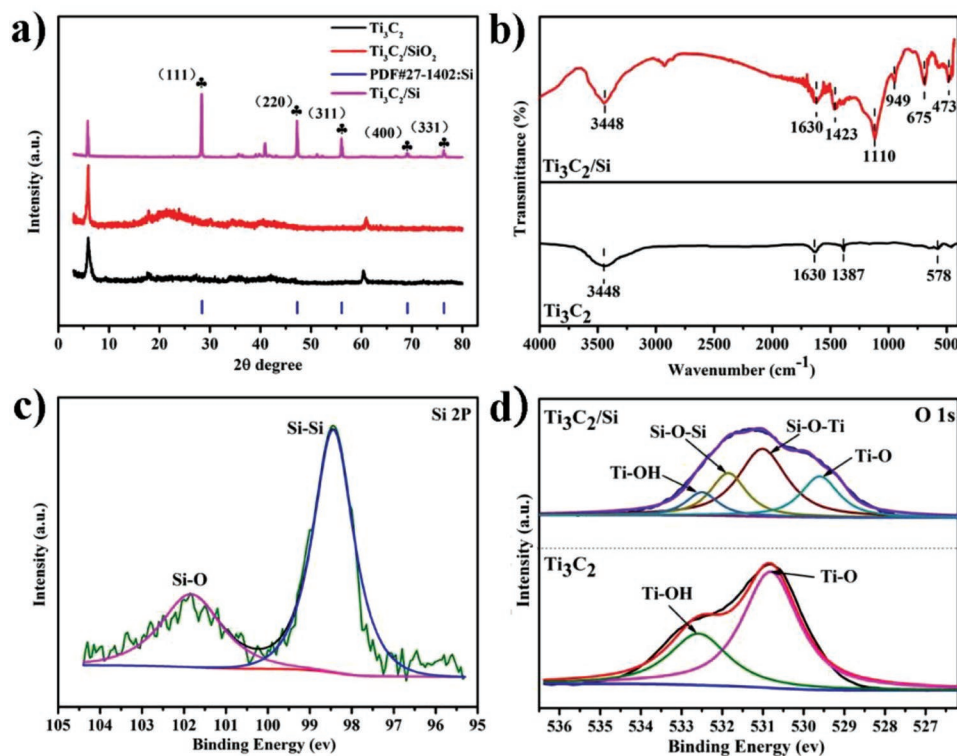
Figure 3. Detailed structural and compositional characterization. a) XRD pattern. b) FTIR spectra. c) Si2p and d) O1s XPS spectra.

lattice image (Figure 2g) presents a lattice spacing of 0.31 nm, corresponding to (111) plane of Si. The selected area electron diffraction (SAED) pattern (Figure 2h) shows distinct diffraction rings related to (111), (220), (311) planes of Si and diffraction spot of Ti_3C_2 related to its hexagonal crystal structure, further indicating the successful hybridization of Ti_3C_2 MXene and Si nanoparticles. It should be noted that the original hexagonal crystal structure of MXene (Figure S4, Supporting Information) is kept in the Ti_3C_2/Si composites. Figure 2k shows Si element mapping image on Ti_3C_2 MXene, which is in accordance with the distribution of homogeneous Si in Figure 2i. Energy dispersive spectrometer (EDS) elemental mapping images in Figure 2i–m and Figure S5 (Supporting Information) demonstrate Si and Ti_3C_2 MXene are successfully coupled.

X-ray diffraction (XRD) patterns in Figure 3a show the crystallinity and phase component of the Ti_3C_2/Si nanosheets. As shown in Figure 3a, the strong peak at 6.0° corresponds to (002) plane of Ti_3C_2, which is in accordance with the reported literature.[46–48] After the hydrolysis of TEOS, new wide peak at 21° attributed to amorphous SiO_2 is observed in Ti_3C_2/SiO_2. As for Ti_3C_2/Si sample, five sharp diffraction peaks of the XRD pattern are assigned to (111), (220), (311), (400), and (331) planes of cubic structured Si (PDF#27-1402), and the peak at 21° of amorphous SiO_2 disappears, indicating the successful reduction from amorphous SiO_2 to crystalline Si after the LTMRR process. This transformation is also confirmed by Raman spectra (Figure S6a, Supporting Information), a strong Stokes shift is observed at 510 cm⁻¹, corresponding to typical Raman characteristics of crystalline Si. Interestingly, the Raman spectrum displays a strong defect-induced (D) peak, and the

intensity ratio (I_D/I_G) of D band and G band is as high as 1.02, suggesting that Ti_3C_2 is full of defects, which can provide more active sites for redox reaction kinetics and for Li⁺ ion insertion/extraction process. Furthermore, Ti_3C_2/Si nanocomposites still remain the typical diffraction peaks at 6.0° corresponding to (002) plane of Ti_3C_2 MXene, demonstrating the LTMRR process does not change the layered structure of Ti_3C_2 MXene.

To reveal the chemical bonding state between Si and MXene Ti_3C_2, an evolution of surface groups is investigated via FTIR spectra (Figure 3b). For both pure MXene Ti_3C_2 and Ti_3C_2/Si samples, characteristic peaks around 3448 and 1630 cm⁻¹ are observed, which are attributed to the stretching vibration of O−H and C=O bonds, respectively.[31] The two bands at 1110 and 473 cm⁻¹ are assignable to Si−O−Si asymmetric stretching and bending vibration. Besides those, there are two newly formed peaks located at 675 and 949 cm⁻¹ for Ti_3C_2/Si sample, which correspond to Ti−O−Ti and Si−O−Ti bond,[49] respectively. The presence of Si−O−Ti bond suggests that there forms chemical bonding between Si and Ti_3C_2 nanosheets, which is stronger than physical combination. The covalent linkage is of great significance for improving the structural stability of the composites.

The chemical bonding state of the Ti_3C_2/Si composite is further investigated by X-ray photoelectron spectroscopy (XPS). A typical XPS survey spectrum (Figure S6b, Supporting Information) confirms the presence of C, Ti, and Si. Comparing the difference between Si 2p XPS spectra of Ti_3C_2/SiO_2 (Figure S6c, Supporting Information) and Ti_3C_2/Si (Figure 3c), we can see that one peak at 103.5 eV attributed to SiO_2-$n$$H_2O$ in Ti_3C_2/SiO_2 converts into two peaks at 98.5 and 101.8 eV, corresponding to

Si—Si and Si—O, once more suggesting the successful reduction from SiO$_2$ to Si. High-resolution O 1s XPS spectrum (Figure 3d) reveals the peaks at 532.5, 531.8, 531.0, and 529.5 eV corresponding to different O states, i.e., Ti—O—H, Si—O—Si, Si—O—Ti, and Ti—O, respectively. The special O valence state (Si—O—Ti at 531.0 eV) indicates the chemical bonding between Si and Ti$_3$C$_2$ MXene, in accordance with the results of FTIR (Figure 3b). To characterize the surface area and pore diameter parameters, the N$_2$-Brunauer–Emmett–Teller adsorption/desorption isotherms are examined. The Si nanoparticles and in-Ti$_3$C$_2$ nanosheets display a specific surface area of 23.54 and 20.01 m^2 g^{-1}, respectively (Figure S7, Supporting Information). Compared with pure Si nanoparticles, the Ti$_3$C$_2$/Si shows a much higher specific area of 34.5 m^2 g^{-1} (Figure S8a, Supporting Information) because of the introduction of lamellar Ti$_3$C$_2$ MXene. Besides, the pore size distribution (Figure S8b, Supporting Information) indicates the presence of micro- and mesopores in the Ti$_3$C$_2$/Si nanocomposites, which can promote the Li$^+$ storage performance by enabling fast Li$^+$ diffusion in electrodes.
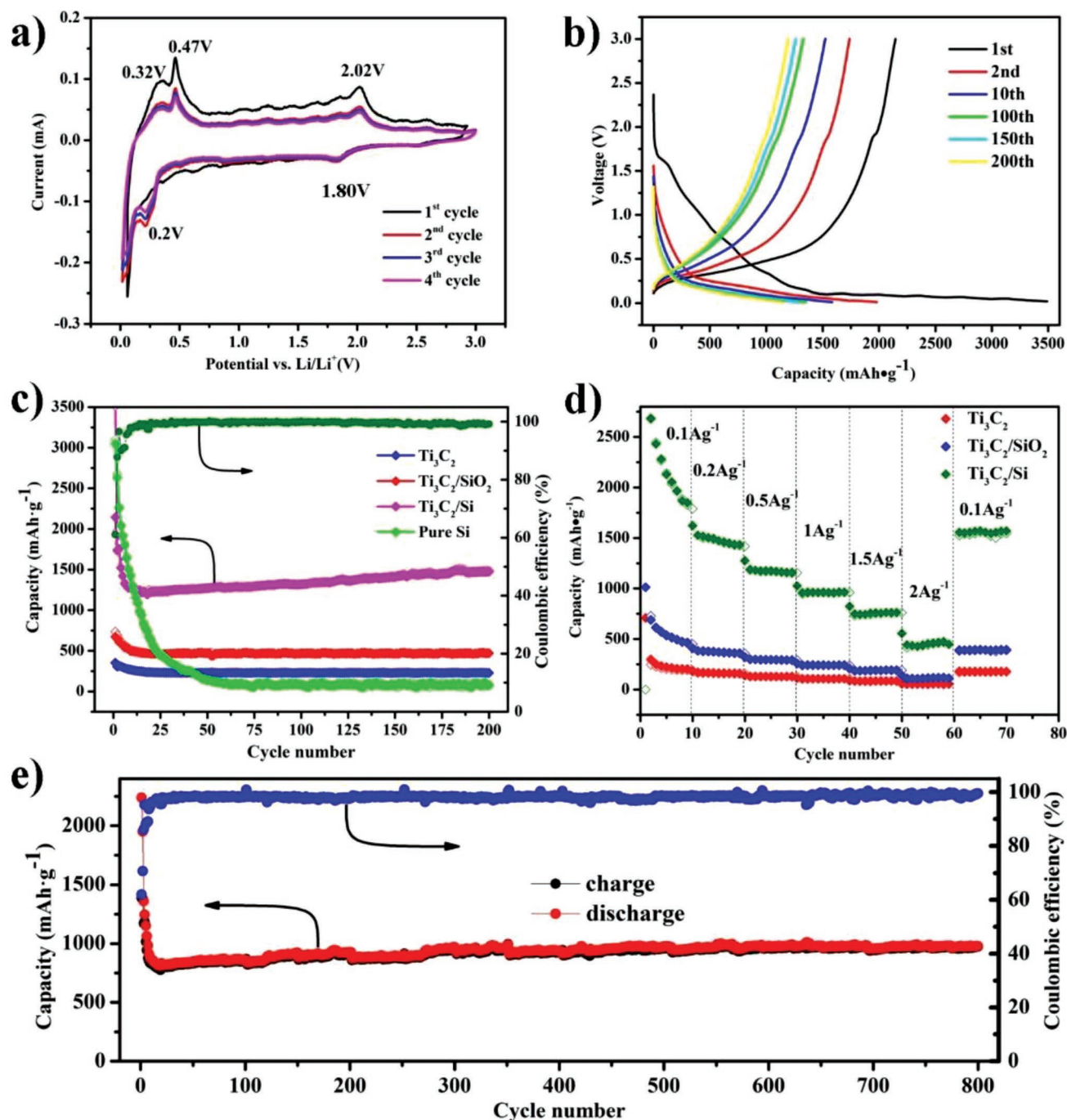
To estimate the electrochemical activity of the lamellar porous Ti$_3$C$_2$/Si anodes for LIBs, the first four cyclic voltammograms (CV) curves at a sweep rate 0.1 mV s^{-1} are presented in **Figure 4**a. For a comparison, pure Ti$_3$C$_2$ electrode is also examined under the same condition (Figure S9a, Supporting Information). Specifically, a reduction peak at 1.8 V is observed in the cathodic scan, corresponding to the formation of solid electrolyte interphase (SEI) layer and the interaction between Li$^+$ and surface functional group of Ti$_3$C$_2$ MXene. Moreover, an obvious reduction peak at around 0.20 V appears at the second cycle, attributing to the reduction of Si to Li$_x$Si phase. In the anodic scans, two well-resolved peaks at 0.32 and 0.47 V can be observed, which are related to the phase transformation process from Li$_x$Si alloy to amorphous Si. More significantly, the CV curves remain unchanged after the second cycle, suggesting a good cycling stability of the Ti$_3$C$_2$/Si electrode. The ex situ XRD patterns (Figure S9b, Supporting Information) of Ti$_3$C$_2$/Si electrode at different charge/discharge stages also confirm above reaction mechanism. As shown in Figure S9b of the Supporting Information, when the cell with Ti$_3$C$_2$/Si electrode is first discharged to 0.01 V, the (111) peak of Si nanoparticles disappears, and the (422) peak of Li$_{21}$Si$_5$ at 23.1° is clearly observed, which can be attributed to the alloying reaction between Si and Li$^+$. Simultaneously, the shift to a lower angle of the (002) peak indicates the enlargement of Ti$_3$C$_2$ MXene interlayer space, which is related to the intercalation of Li$^+$ into MXene. As for the delithiation process, when the cell is charged to 3.0 V, the Li$_{21}$Si$_5$ peak disappears, but the (111) peak of Si does not appear again, suggesting the conversion from crystalline Si to amorphous Si. It should be noted that the interlayer space of Ti$_3$C$_2$ MXene does not change basically during the delithiation process.

The CV results show that the electrochemical reactivity of the Ti$_3$C$_2$/Si electrode is in good accordance with the discharge/charging profiles, as shown in Figure 4b. The first discharge and charge capacities are 3512.5 and 2145.1 mAh g^{-1}, respectively, corresponding to a coulombic efficiency of 61.1% at 100 mA g^{-1}. This irreversible capacity loss is mainly caused by the electrochemically activated decomposition of electrolyte that results in the formation of the SEI layer. However, the

coulombic efficiency soars to 87.8% at the second cycle. From the 10th cycle on, the coulombic efficiency remains unchanged basically, indicating the highly reversible Li$^+$ storage behavior of the Ti$_3$C$_2$/Si nanosheets.

The cycle performance and cycle stability of Ti$_3$C$_2$, Ti$_3$C$_2$/SiO$_2$, Ti$_3$C$_2$/Si, and commercial Si anodes at a current density of 100 mA g^{-1} are further investigated (Figure 4c). To guarantee the rationality of performance comparison, we purchased the commercial Si nanoparticles with similar size (Figure S10a, Supporting Information), and the XRD pattern (Figure S10b, Supporting Information) reveals its good crystallinity. Obviously, the capacity of pure Si electrode fades rapidly, which can be attributed to the serious volume expansion. By contrast, the Ti$_3$C$_2$/Si electrode exhibits markedly improved cycle stability, retaining 1475 mAh g^{-1} at 100 mA g^{-1} after 200 cycles without obvious attenuation from 10th cycle on, corresponding to the high volumetric capacity of 3540.7 mAh cm^{-3}, which is much higher than that of commercial graphite anode (370 mAh cm^{-3}).[50] This capacity is also apparently superior to those of Ti$_3$C$_2$/SiO$_2$ (470.2 mAh g^{-1}) and Ti$_3$C$_2$ (228.7 mAh g^{-1}) electrodes. The fast capacity fading in the initial 10 cycles mainly attributes to the Li$^+$ consumption caused by the formation of SEI layer[51–54] and the decomposition of electrolyte in initial several cycles.[55] It is noted that capacity in this work is calculated based on the mass of the total electrode (Ti$_3$C$_2$ + Si). The high specific capacity of Ti$_3$C$_2$/Si anode should be ascribed to the outstanding electrochemical activity of Si nanoparticles and the indispensable synergistic action of Ti$_3$C$_2$ MXene. The rate performance of Ti$_3$C$_2$/Si electrode from 100 mA g^{-1} to 2A g^{-1} is shown in Figure 4d. The capacity gradually decreases from 1849 to 467 mAh g^{-1} with the current density increasing from 100 mA g^{-1} to 2 A g^{-1}. It should be stressed that after abruptly switching the initial current density back to 100 mA g^{-1}, a large capacity of 1556 mAh g^{-1} is regained, demonstrating the excellent rate performance of Ti$_3$C$_2$/Si anode. In sharp contrast, at each current density, Ti$_3$C$_2$/Si all exhibits much higher capacity than Ti$_3$C$_2$ and Ti$_3$C$_2$/SiO$_2$ electrodes, indicating the coupling of the Ti$_3$C$_2$ MXene with Si nanoparticles is favorable to the performance improvement.

Furthermore, long-term cycle stability of Ti$_3$C$_2$/Si is tested at 1 A g^{-1} (Figure 4e), Ti$_3$C$_2$/Si electrode delivered a high reversible capacity of 973 mAh g^{-1} after 800 cycles, revealing excellent cycling stability, which is superior to those of other previously reported Ti$_3$C$_2$-based and Si-based anodes (Table S1, Supporting Information). The SEM and TEM images (Figure S11, Supporting Information) suggest the structural stability of the Ti$_3$C$_2$/Si nanocomposite after the long cycle, the Si nanoparticles are uniformly dispersed on the surface of MXene. Above results should be attributed to the unique lamellar mesoporous nanostructure of Ti$_3$C$_2$/Si electrode, which offer a good conductive network for Li$^+$ ions and electrons transport and a buffer to accommodate the volume expansion of nanoscale Si. In order to examine the structural stability and buffer action of Ti$_3$C$_2$ MXene, the cycled batteries are disassembled after 50 cycles to reveal the morphological changes of Ti$_3$C$_2$/Si and pure Si anodes. For the cycled pure Si anode, the active materials are powdered and separated from the collector because of the huge and irreversible volume expansion of Si during lithiation/delithiation process (Figure S12a–d, Supporting Information).

Figure 4. Electrochemical and lithium ion storage performance. a) Initial fore CV curves (sweep rate = 0.1 mV s^{-1}) of Ti$_3$C$_2$/Si electrode. b) Charging/discharging voltage profiles (current density = 100 mA g^{-1}) of Ti$_3$C$_2$/Si electrode. c) The specific capacity at 100 mA g^{-1} of Ti$_3$C$_2$, Ti$_3$C$_2$/SiO$_2$, Ti$_3$C$_2$/Si, and pure Si electrodes. d) The rate performance of Ti$_3$C$_2$, Ti$_3$C$_2$/SiO$_2$, and Ti$_3$C$_2$/Si electrodes. e) Long cycle performance (at 1 A g^{-1} for 800 cycles) of Ti$_3$C$_2$/Si electrode.

SEM images (Figure S12e,f, Supporting Information) exhibit that cracks appear on the previously flat and compact surface of Si electrode after 50 cycles. Figure S12g,h of the Supporting Information shows the cross-sectional SEM images of the pure Si electrodes before and after cycling. The Si anode exhibits tremendous thickness change of 217.7% from 3.49 to 11.09 μm.

By contrast, for the cycled Ti$_3$C$_2$/Si electrode, the surface of electrode still remains integral with no obvious damage after 50 cycles, the separator maintains bright white colors with no particle adhered (Figure S13a–d, Supporting Information). The SEM images (Figure S13e,f, Supporting Information) reveal that the microsurface of Ti$_3$C$_2$/Si anode does not show

**ADVANCED
SCIENCE NEWS**

www.advancedsciencenews.com

**ADVANCED
ENERGY
MATERIALS**

www.advenergymat.de

any apparent disintegration as well. As shown in the cross-sectional SEM images (Figure S13g,h, Supporting Information), Ti_3C_2/Si electrode with a thickness of 4.42 µm exhibits thickness increase of 6.79%, which is far less than that of pure Si electrode. Above results suggest the stable hierarchical porous nanostructure of Ti_3C_2/Si plays an extremely significant role in reliving the volume expansion and keeping the structural integrality of electrode.

To investigate the influence of Si content on the electrochemical performance, Ti_3C_2/Si samples with three different Si contents are synthesized by controlling the dose of TEOS (as labeled as Ti_3C_2/Si-1, Ti_3C_2/Si-2, Ti_3C_2/Si-3). The Si content of the as-prepared samples can be determined via inductive coupled plasma emission spectrometer. As shown in Figure S14a–d of the Supporting Information, the Si content of Ti_3C_2/Si-1, Ti_3C_2/Si-2, and Ti_3C_2/Si-3 is 25.4%, 38.3%, and 58.3%, respectively, approximately equal to the EDS result (Figure S15, Supporting Information). As shown in Figure S14e and Table S2 of the Supporting Information, the first discharge capacity increases with Si content, while the initial coulombic efficiency decreases with Si content contrarily, because the increased Si contents provide higher capacity but the agglomeration of Si particles independent of Ti_3C_2 makes it difficult to form the stable SEI layer. Besides, after 100 cycles, the specific capacity of Ti_3C_2/Si-3 is lower than that of Ti_3C_2/Si-2, indicating the poorer cyclic stability of Ti_3C_2/Si-3. Because in the Ti_3C_2/Si-3 electrode, the volume expansion of aggregate Si particles weakens the function of Ti_3C_2 MXene in buffering the volume change. Ti_3C_2/Si-1 shows lower specific capacity, which could be caused by the lower Si content, resulting in more restacked Ti_3C_2 MXene layers. The compact and restacked MXene layers make against the ion transport and electrolyte infiltration.
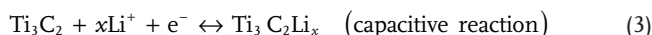
The reaction kinetics could be investigated by electrochemical impedance spectroscopy (EIS). As shown in **Figure 5**a, a semicircle in the high frequency region corresponds to the contact resistance and charge transfer resistance (R_{ct}), and a sloping line in the low frequency region is related to the ion diffusion ability within the electrodes, making up the Nyquist plot. The R_{ct} value of Ti_3C_2/Si electrode is the lowest one (82 Ω) compared to those of Ti_3C_2 (183 Ω), Ti_3C_2/SiO_2 (217 Ω), and pure Si (298 Ω) electrodes, suggesting that Ti_3C_2/Si anode displays the smallest charge transfer resistance among these anodes, revealing enhanced reaction kinetics of Ti_3C_2/Si electrode. Figure 5b exhibits the relationship between the impedance and the phase angle. Smaller slope ($\tan\theta_1$) of Ti_3C_2/Si than that of pure Si ($\tan\theta_2$) demonstrates that the Ti_3C_2/Si sample displays a smaller Warburg factor, corresponding to the larger Li^+ ion diffusion coefficient. It might be contributed to the excellent Li^+ diffusion mobility of Ti_3C_2/Si with lamellar porous structure and the short Li^+ ion transport length in the porous structures.

Ti_3C_2 MXene possesses significant pseudocapacitive property due to the surface redox reactions, which takes effect in capacity contribution. To further study the Li^+ storage mechanism in the Ti_3C_2/Si electrode, CV measurements at different sweep rates (0.1–1 mV s^{-1}) are conducted, as shown in Figure 5c. Here, the Li^+ storage mechanism mainly includes three types: diffusion contribution from alloying reaction, capacitive contribution based on the surface redox reactions, and capacitive contribution from the double layer charging.[56,57] The capacitive effect plays

a substantial role in energy storage for high surface area materials. The capacitive contribution can be determined by the relationship between the measured current (i) and the scan rate (v)

$$i = av^b \tag{1}$$

Both a and b are adjustable factors. Generally, $b = 0.5$ corresponds to a diffusion-controlled process (battery-model energy storage mechanism), while $b = 1$ relates to a fully capacitive-controlled process (capacitive-model energy storage mechanism).[57,58] According to the results of CV measurement as shown in Figure 5c, the b values of anodic (peak A) and cathodic peak (peak B) are calculated to be 0.69 and 0.68 (Figure 5d), which suggests that the capacitive-model energy storage mechanism cannot be ignored in the Ti_3C_2/Si electrode. On the basis of the relationship between current value $i(v)$ at fixed voltage, capacity contribution (k_1v), and diffusion contribution ($k_2v^{1/2}$): $i(v) = k_1v + k_2v^{1/2}$, the capacitive contribution from the total Li^+ storage can be confirmed quantitatively.[58] As an example, 35.3% of capacitive contribution to the total Li^+ storage can be figured out at the sweep rate of 0.7 mV s^{-1}, as shown in Figure 5e. Moreover, the proportion of capacitive-controlled capacity increases with the sweep rate (Figure 5f), illustrating that the capacitive behavior can be useful for store/release Li^+ more effectively at higher sweep rate, due to the rapid charge/discharge characteristic of the capacitive storage mechanism. These results indicate that the energy storage process of Ti_3C_2/Si nanocomposite anode defers to a battery-capacitive dual-model energy storage mechanism (Figure S16, Supporting Information)[37]

$$Si + xLi^+ + e^- \leftrightarrow Li_xSi \quad (battery\ reaction) \tag{2}$$

$$Ti_3C_2 + xLi^+ + e^- \leftrightarrow Ti_3C_2Li_x \quad (capacitive\ reaction) \tag{3}$$

Primarily, the Si nanoparticles contribute to the battery part through Li–Si alloy reaction for high capacity energy storage (reaction (2)). Ti_3C_2 MXene contributes to capacitive part (reaction (3)) through surface redox reaction. Furthermore, the covalent linkage (Si—O—Ti bonds) between Ti_3C_2 MXene and Si nanoparticles makes great difference as a double-assistance. For the battery-model storage, it provides efficient interfacial charge transfer and high interfacial mechanical stability. For the pseudocapacitive storage, the Si—O—Ti bonds further polarize atomic charge within the composite, which can enhance the adsorption of Li^+ ion.[37] Above factors jointly bring up the outstanding electrochemical performance of batteries.

3. Conclusions

Herein, we report a novel and efficient strategy integrating in situ orthosilicate hydrolysis and low-temperature reduction process to synthesize Si/Ti_3C_2 MXene composites. The synthesized Si/Ti_3C_2 MXene composite presents the superiorities of increased active surface area, enhanced charge transfer kinetics, and favorable structural stability, greatly enhancing lithium ion storage performance in terms of stability, rate ability, and capacity. Ti_3C_2 MXene not only provides fast transfer channels
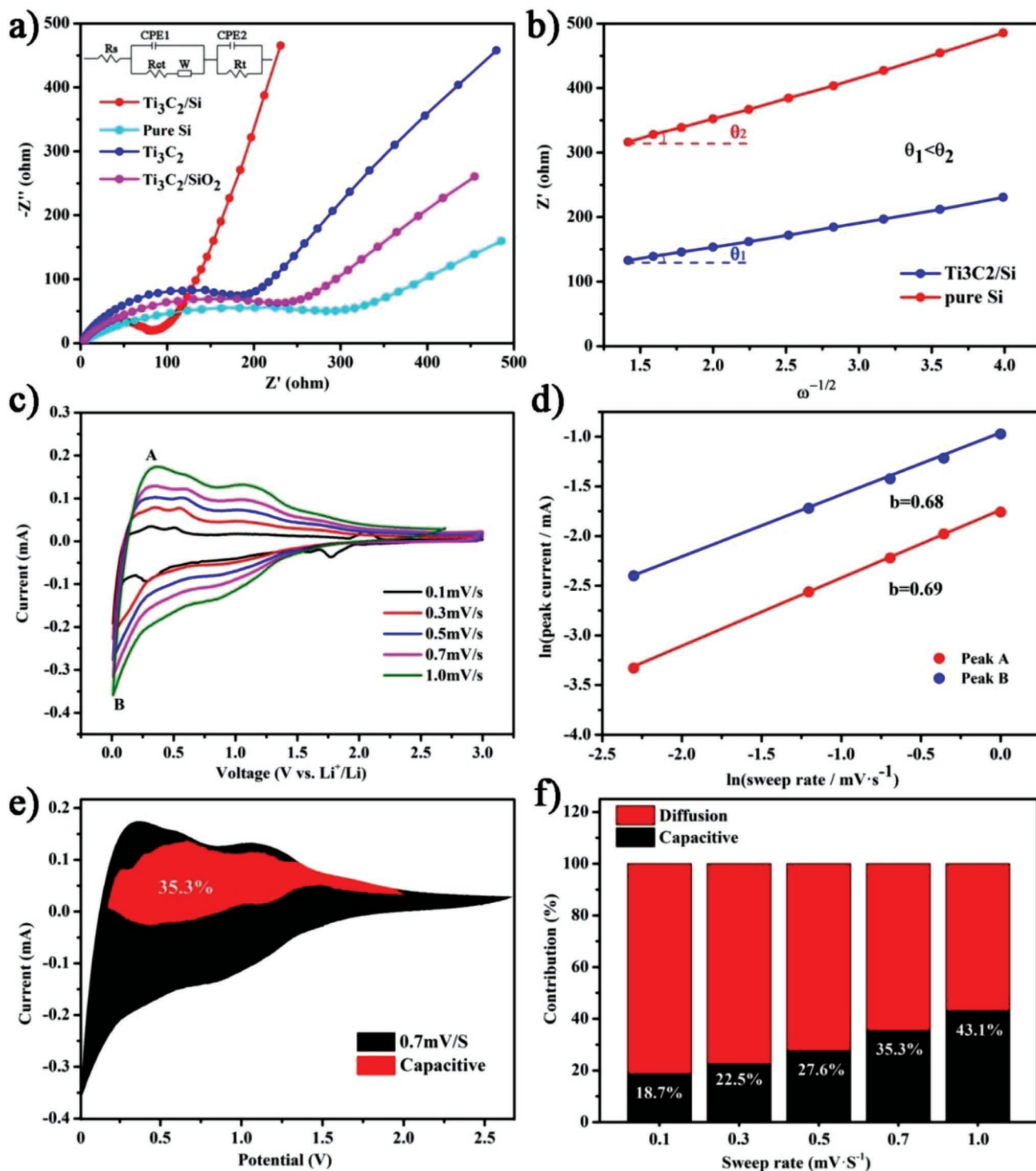
Figure 5. Kinetics analysis of the electrochemical behavior. a) EIS spectrum. b) Relationship between Zre and $\omega^{1/2}$ in the low-frequency region. c) CV curves of the Ti_3C_2/Si electrode at different sweep rate (0.1–1 mV s^{-1}). d) Relationship between peak current and sweep rate (plotted with natural logarithm axis). e) CV curve with corresponding capacitive contribution at 0.7 mV s^{-1}. f) Capacitive contribution ratios at different sweep rate.

for Li$^+$ and electrons, but also relieves volume expansion of Si during cycling as an efficient buffer. Moreover, the characteristics of excellent pseudocapacitive behavior and abundant surface redox reaction sites of Ti_3C_2 MXene can synergistically

contribute to energy storage performance enhancement. As expected, Ti_3C_2/Si anode exhibits outstanding specific capacity of 1849 mAh g^{-1} at 100 mA g^{-1}, even retaining 956 mAh g^{-1} at 1 A g^{-1}. The in situ low-temperature synthetic route to Si/Ti_3C_2

MXene electrodes and involved battery-capacitive dual-model energy storage mechanism can be potential for designing novel high-performance electrodes for energy storage devices.

4. Experimental Section

Experimental Section and any associated references are available in the Supporting Information.

Supporting Information

Supporting Information is available from the Wiley Online Library or from the author.

Conflict of Interest

The authors declare no conflict of interest.

[1] M. Ge, J. Rong, X. Fang, C. Zhou, *Nano Lett.* **2012**, *12*, 2318.
[2] H. Jia, P. Gao, J. Yang, J. Wang, Y. Nuli, Z. Yang, *Adv. Energy Mater.* **2011**, *1*, 1036.
[3] L. Lin, X. Xu, C. Chu, M. K. Majeed, J. Yang, *Angew. Chem., Int. Ed.* **2016**, *55*, 14063.
[4] Y. He, X. Yu, Y. Wang, H. Li, X. Huang, *Adv. Mater.* **2011**, *23*, 4938.
[5] Z. Chen, J. W. F. To, C. Wang, Z. Lu, N. Liu, A. Chortos, L. Pan, F. Wei, Y. Cui, Z. Bao, *Adv. Energy Mater.* **2014**, *4*, 1400207.
[6] J. Ryu, T. Chen, T. Bok, G. Song, J. Ma, C. Hwang, L. Luo, H. K. Song, J. Cho, C. Wang, S. Zhang, S. Park, *Nat. Commun.* **2018**, *9*, 2924.
[7] X. Su, Q. Wu, J. Li, X. Xiao, A. Lott, W. Lu, B. W. Sheldon, J. Wu, *Adv. Energy Mater.* **2014**, *4*, 1300882.
[8] G. Zhang, Y. Yang, Y. Chen, J. Huang, T. Zhang, H. Zeng, C. Wang, G. Liu, Y. Deng, *Small* **2018**, *14*, 1801189.
[9] D. Yao, Y. Yang, Y. Deng, C. Wang, *J. Power Sources* **2018**, *379*, 26.
[10] H. Kim, M. Seo, M. H. Park, J. Cho, *Angew. Chem., Int. Ed.* **2010**, *49*, 2146.
[11] L.-F. Cui, R. Ruffo, C. K. Chan, H. Peng, Y. Cui, *Nano Lett.* **2009**, *9*, 491.
[12] H. Wu, G. Chan, J. W. Choi, I. Ryu, Y. Yao, M. T. McDowell, S. W. Lee, A. Jackson, Y. Yang, L. Hu, Y. Cui, *Nat. Nanotechnol.* **2012**, *7*, 310.
[13] P. R. Abel, Y. M. Lin, H. Celio, A. Heller, C. B. Mullins, *ACS Nano* **2012**, *6*, 2506.
[14] N. Liu, J. Liu, D. Jia, Y. Huang, J. Luo, X. Mamat, Y. Yu, Y. Dong, G. Hu, *Energy Storage Mater.* **2019**, *18*, 165.
[15] Y. Wang, H. Li, P. He, E. Hosono, H. Zhou, *Nanoscale* **2010**, *2*, 1294.
[16] M. Pramanik, Y. Tsujimoto, V. Malgras, S. X. Dou, J. H. Kim, Y. Yamauchi, *Chem. Mater.* **2015**, *27*, 1082.
[17] L. Pan, H. Huang, M. Zhong, M. Niederberger, *Energy Storage Mater.* **2019**, *16*, 519.
[18] S. M. Hwang, Y.-G. Lim, J.-G. Kim, Y.-U. Heo, J. H. Lim, Y. Yamauchi, M.-S. Park, Y.-J. Kim, S. X. Dou, J. H. Kim, *Nano Energy* **2014**, *10*, 53.
[19] W. J. Lee, T. H. Hwang, J. O. Hwang, H. W. Kim, J. Lim, H. Y. Jeong, J. Shim, T. H. Han, J. Y. Kim, J. W. Choi, S. O. Kim, *Energy Environ. Sci.* **2014**, *7*, 621.
[20] B. Wang, X. Li, X. Zhang, B. Luo, Y. Zhang, L. Zhi, *Adv. Mater.* **2013**, *25*, 3560.
[21] Q. Xu, J.-K. Sun, Y.-X. Yin, Y.-G. Guo, *Adv. Funct. Mater.* **2018**, *28*, 1705235.
[22] Q. Xu, J. K. Sun, G. Li, J. Y. Li, Y. X. Yin, Y. G. Guo, *Chem. Commun.* **2017**, *53*, 12080.
[23] Q. Xu, J.-Y. Li, J.-K. Sun, Y.-X. Yin, L.-J. Wan, Y.-G. Guo, *Adv. Energy Mater.* **2017**, *7*, 1601481.
[24] M. Ko, S. Chae, J. Ma, N. Kim, H.-W. Lee, Y. Cui, J. Cho, *Nat. Energy* **2016**, *1*, 16113.
[25] S. Zhu, J. Zhou, Y. Guan, W. Cai, Y. Zhao, Y. Zhu, L. Zhu, Y. Zhu, Y. Qian, *Small* **2018**, *14*, 1802457.
[26] J. Chang, X. Huang, G. Zhou, S. Cui, P. B. Hallac, J. Jiang, P. T. Hurley, J. Chen, *Adv. Mater.* **2014**, *26*, 758.
[27] Q. Xu, J. K. Sun, Z. L. Yu, Y. X. Yin, S. Xin, S. H. Yu, Y. G. Guo, *Adv. Mater.* **2018**, *30*, 1707302.
[28] F. Kong, X. He, Q. Liu, X. Qi, Y. Zheng, R. Wang, Y. Bai, *Ceram. Int.* **2018**, *44*, 11591.
[29] D. Er, J. Li, M. Naguib, Y. Gogotsi, V. B. Shenoy, *ACS Appl. Mater. Interfaces* **2014**, *6*, 11173.
[30] Q. Tang, Z. Zhou, P. Shen, *J. Am. Chem. Soc.* **2012**, *134*, 16909.
[31] R. Zhao, M. Wang, D. Zhao, H. Li, C. Wang, L. Yin, *ACS Energy Lett.* **2018**, *3*, 132.
[32] C. Yang, Y. Tang, Y. Tian, Y. Luo, M. Faraz Ud Din, X. Yin, W. Que, *Adv. Energy Mater.* **2018**, *8*, 1802087.
[33] M.-Q. Zhao, M. Torelli, C. E. Ren, M. Ghidiu, Z. Ling, B. Anasori, M. W. Barsoum, Y. Gogotsi, *Nano Energy* **2016**, *30*, 603.
[34] B. Ahmed, D. H. Anjum, Y. Gogotsi, H. N. Alshareef, *Nano Energy* **2017**, *34*, 249.
[35] B. Li, D. Zhang, Y. Liu, Y. Yu, S. Li, S. Yang, *Nano Energy* **2017**, *39*, 654.
[36] M. Guo, C. Liu, Z. Zhang, J. Zhou, Y. Tang, S. Luo, *Adv. Funct. Mater.* **2018**, *28*, 1803196.
[37] R. Meng, J. Huang, Y. Feng, L. Zu, C. Peng, L. Zheng, L. Zheng, Z. Chen, G. Liu, B. Chen, Y. Mi, J. Yang, *Adv. Energy Mater.* **2018**, *8*, 1801514.
[38] F. Kong, X. He, Q. Liu, X. Qi, D. Sun, Y. Zheng, R. Wang, Y. Bai, *Electrochem. Commun.* **2018**, *97*, 16.
[39] Y. Zhang, Z. Mu, J. Lai, Y. Chao, Y. Yang, P. Zhou, Y. Li, W. Yang, Z. Xia, S. Guo, *ACS Nano* **2019**, *13*, 2167.
[40] C. J. Zhang, S. H. Park, A. Seral-Ascaso, S. Barwich, N. McEvoy, C. S. Boland, J. N. Coleman, Y. Gogotsi, V. Nicolosi, *Nat. Commun.* **2019**, *10*, 849.

[41] J. Wang, J. Tang, B. Ding, V. Malgras, Z. Chang, X. Hao, Y. Wang, H. Dou, X. Zhang, Y. Yamauchi, *Nat. Commun.* **2017**, *8*, 15717.

[42] H. Xue, J. Zhao, J. Tang, H. Gong, P. He, H. Zhou, Y. Yamauchi, J. He, *Chem. - Eur. J.* **2016**, *22*, 4915.

[43] S. Yang, X. Feng, L. Wang, K. Tang, J. Maier, K. Mullen, *Angew. Chem., Int. Ed.* **2010**, *49*, 4795.

[44] N. Lin, Y. Han, J. Zhou, K. Zhang, T. Xu, Y. Zhu, Y. Qian, *Energy Environ. Sci.* **2015**, *8*, 3187.

[45] A. Lipatov, M. Alhabeb, M. R. Lukatskaya, A. Boson, Y. Gogotsi, A. Sinitskii, *Adv. Electron. Mater.* **2016**, *2*, 1600255.

[46] X. Xie, Y. Xue, L. Li, S. Chen, Y. Nie, W. Ding, Z. Wei, *Nanoscale* **2014**, *6*, 11035.

[47] M. Ghidiu, M. R. Lukatskaya, M. Q. Zhao, Y. Gogotsi, M. W. Barsoum, *Nature* **2014**, *516*, 78.

[48] O. Mashtalir, M. Naguib, V. N. Mochalin, Y. Dall'Agnese, M. Heon, M. W. Barsoum, Y. Gogotsi, *Nat. Commun.* **2013**, *4*, 1716.

[49] Z. Li, H. Zhao, P. Lv, Z. Zhang, Y. Zhang, Z. Du, Y. Teng, L. Zhao, Z. Zhu, *Adv. Funct. Mater.* **2018**, *28*, 1605711.

[50] S. Jeong, J. P. Lee, M. Ko, G. Kim, S. Park, J. Cho, *Nano Lett.* **2013**, *13*, 3403.

[51] M. Lu, W. Han, H. Li, W. Shi, J. Wang, B. Zhang, Y. Zhou, H. Li, W. Zhang, W. Zheng, *Energy Storage Mater.* **2019**, *16*, 163.

[52] M. Q. Zhao, X. Xie, C. E. Ren, T. Makaryan, B. Anasori, G. Wang, Y. Gogotsi, *Adv. Mater.* **2017**, *29*, 1702410.

[53] J. Li, D. Yan, S. Hou, Y. Li, T. Lu, Y. Yao, L. Pan, *J. Mater. Chem. A* **2018**, *6*, 1234.

[54] X. Sang, Y. Xie, D. E. Yilmaz, R. Lotfi, M. Alhabeb, A. Ostadhossein, B. Anasori, W. Sun, X. Li, K. Xiao, P. R. C. Kent, A. C. T. van Duin, Y. Gogotsi, R. R. Unocic, *Nat. Commun.* **2018**, *9*, 2266.

[55] Y. Ma, R. Younesi, R. Pan, C. Liu, J. Zhu, B. Wei, K. Edström, *Adv. Funct. Mater.* **2016**, *26*, 6797.

[56] T. C. Liu, W. Pell, B. Conway, S. Roberson, *J. Electrochem. Soc.* **1998**, *145*, 1882.

[57] J. Wang, J. Polleux, J. Lim, B. Dunn, *J. Phys. Chem. C* **2007**, *111*, 14925.

[58] T. Brezesinski, J. Wang, S. H. Tolbert, B. Dunn, *Nat. Mater.* **2010**, *9*, 146.